A Compact Single-Resonator Dual-Port Circularly Polarized MIMO Dielectric Resonator Antenna for 28 GHz Applications

electronics

MDPI

Article

A Compact Single-Resonator Dual-Port Circularly Polarized MIMO Dielectric Resonator Antenna for 28 GHz Applications

Sumer Singh Singhwal [1] and Ladislau Matekovits [1,2,3,*]

[1] Department of Electronics and Telecommunications (DET), Politecnico di Torino, 10129 Turin, Italy; sumer.singhwal@polito.it
[2] Istituto di Elettronica e di Ingegneria dell'Informazione e delle Telecomunicazioni, National Research Council of Italy, 10129 Turin, Italy
[3] Department of Measurements and Optical Electronics, University Politehnica Timişoara, 300006 Timisoara, Romania
* Correspondence: ladislau.matekovits@polito.it

Abstract

A compact dual-port circularly polarized (CP) multiple-input multiple-output (MIMO) dielectric resonator antenna (DRA) for 28 GHz applications is presented. A single cross-shaped dielectric resonator is excited by two orthogonal microstrip feeds, supporting hybrid orthogonal modes that enable CP radiation at both ports without requiring perturbation cuts, parasitic elements, or decoupling structures. The fabricated prototype exhibits a measured 10 dB impedance bandwidth and 3 dB axial ratio bandwidth that fully cover the Federal Communications Commission (FCC)-allocated 28 GHz band (27.5–28.35 GHz). Port isolation remains better than 15 dB, and the antenna exhibits a peak gain of approximately 7.6 dBi with radiation efficiency exceeding 93%, within a compact 40 × 47 mm^2 footprint. MIMO performance is verified through envelope correlation coefficient (ECC), diversity gain (DG), and total active reflection coefficient (TARC). The results demonstrate that the proposed single-resonator dual-port CP DRA provides an efficient and integration-friendly solution for compact mmWave MIMO applications in next-generation 5G/6G terminals.

Keywords: dielectric resonator antenna; multiple input multiple output; 28 GHz; circular polarization

1. Introduction

Multiple-input multiple-output (MIMO) antennas have become a central part of modern wireless platforms, largely because of their ability to improve spectral efficiency, link reliability, and overall channel capacity. As fifth-generation (5G) and sixth-generation (6G) systems continue to push toward higher data rates, lower latency, and denser user connectivity, attention has naturally shifted toward the millimeter wave (mmWave) spectrum. Among the available mmWave allocations, the 28 GHz band (27.5–28.35 GHz) designated by the Federal Communications Commission (FCC) [1] has emerged as an especially attractive candidate for short-range, multi-gigabit links. Operating at such high frequencies, however, also exposes well-known limitations of conventional microstrip antennas: increased conductor loss, strong surface wave excitation, and sensitivity to even small fabrication tolerances. These effects collectively reduce radiation efficiency and aggravate mutual coupling, making compact MIMO integration difficult.

Dielectric resonator antennas (DRAs) offer a promising alternative for mmWave applications. Thanks to their volumetric field confinement and minimal ohmic losses, DRAs

Academic Editor: Hector E. Nistazakis

Received: 16 January 2026
Revised: 20 February 2026
Accepted: 23 February 2026
Published: 27 February 2026

can maintain a high radiation efficiency and wide impedance bandwidth even as electrical size shrinks [2–5]. Their three-dimensional geometry also suppresses surface waves, which naturally helps reduce inter-element coupling—an important advantage when multiple antenna ports must coexist within a limited physical footprint. As a result, DRAs have been explored extensively across microwave and mmWave bands in single-port, multi-port, and polarization-diverse configurations.

Circular polarization (CP) is an additional requirement in many modern communication scenarios. CP antennas are less sensitive to orientation, suffer fewer polarization mismatches, and often provide a more stable performance in multipath-rich environments. Numerous CP MIMO DRA architectures have been reported, using techniques such as perturbed resonators, hybrid or differential feeds, and annular or ring-shaped structures [6,7]. Other studies have introduced electromagnetic bandgap (EBG) inclusions, parasitic strips, and metamaterial or absorber-based layers to suppress mutual coupling and broaden bandwidth [8–10]. While effective, these strategies usually increase the number of dielectric elements, add height, or require intricate feed networks—factors that become restrictive when targeting compact mmWave hardware.

A more space-efficient solution is to generate two orthogonal CP ports using a single dielectric resonator. This concept simplifies modal control, enables a smaller footprint, and provides better symmetry between ports. Despite its appeal, only a limited number of dual-port CP MIMO DRA designs have been reported in the mmWave region. Most existing solutions still depend on perturbation cuts, parasitic elements, or auxiliary isolation structures, and many offer only narrow axial ratio bandwidths.

In this context, the present work introduces a compact dual-port circularly polarized MIMO DRA specifically developed for the 28 GHz band. The antenna features a cross-shaped dielectric resonator excited by two orthogonal microstrip feeds on an RT/Duroid 6002 substrate. By merging four rectangular sections into a single cross-like volume, the resonator supports a pair of near-degenerate orthogonal modes derived from the quasi-TE_{311} family, which naturally produce circular polarization at both ports—without relying on perturbation slots, metallic parasitics, or metasurface-based decouplers. The antenna maintains a high radiation efficiency across the operating band, and the inherent symmetry of the structure yields strong inter-port isolation, despite the absence of any additional decoupling networks. Comprehensive measurements confirm wide overlapping impedance and axial ratio bandwidths that fully cover the 28 GHz allocation, along with stable radiation patterns and favourable MIMO behaviour. The envelope correlation coefficient (ECC) and total active reflection coefficient (TARC), evaluated following the methods of [11–14], remain within the limits expected for efficient MIMO operation. Overall, the proposed design differs from previously reported CP MIMO DRAs in a key respect: it achieves dual-port circular polarization and better than 15 dB port isolation using a single dielectric resonator, with no auxiliary isolation structures. The resulting compactness, efficiency, and polarization purity make the antenna well suited for mmWave MIMO applications and polarization-diverse modules in next-generation communication systems.

2. Antenna Design and Operating Principle

2.1. Antenna Configuration

The geometry of the proposed antenna is shown in Figure 1. A cross-shaped dielectric resonator of height 4.8 mm is mounted on the top surface of an RT/Duroid 6002 substrate. The substrate has relative permittivity $\varepsilon_r = 2.94$, thickness 0.8 mm, and loss tangent $\tan\delta = 0.0012$, while the resonator is machined from Eccostock Hik material with $\varepsilon_r = 10$ and $\tan\delta = 0.001$. A 3-D exploded view of the complete structure is given in Figure 1a. The bottom face of the substrate is completely metallized to form the ground plane; its

outline and the resonator footprint are depicted in Figure 1b. The final substrate size is 40×47 mm^2. The DRA consists of four rectangular arms arranged in a cross around a central square aperture. As indicated in Figure 1c, each arm has a width of 5.85 mm and an effective length of 4.9 mm, whereas the inner square slot measures 3.9 mm on each side. This layout increases the effective electrical path while keeping the occupied volume small. Two orthogonal microstrip feeds are printed on the top side of the substrate, as shown in Figure 1. Each feed is implemented as a bent U-shaped line that terminates underneath one arm of the cross-shaped DRA. The line width is chosen for 50 Ω characteristic impedance, and the bend radii are rounded to reduce discontinuity effects. The ports are placed along adjacent edges of the substrate, leaving space for 2.92 mm end-launch connectors. Two screw holes are provided on opposite corners to facilitate mechanical fixation and to allow straight forward integration of the antenna module inside a larger front-end assembly.

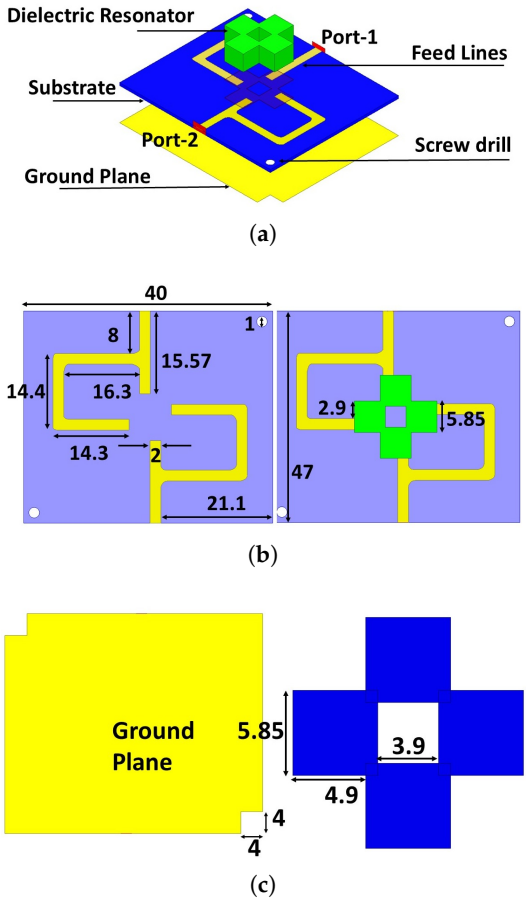

Figure 1. Geometry of the proposed antenna (dimensions in mm): (**a**) layered structure of the dielectric resonator antenna (DRA), (**b**) top view of the microstrip feed layout, (**c**) ground plane with screw holes and cross-shaped dielectric resonator.

2.2. Design Evolution

The dielectric block dimensions were first estimated using Marcatili's approximation [15] for the TE^{z}_{311} mode and then refined through full-wave optimization. A $5.6 \times 5.6 \times 5.6$ mm^3 resonator (Antenna I) resonates close to 28 GHz in eigenmode simulation. When placed on the RT/Duroid 6002 substrate and excited by a microstrip feed, the resonance shifts upward due to dielectric loading and fringing fields, motivating a geometry refinement.

To study modal behavior and coupling, four identical RDRAs were initially arranged and fed (Antenna II) as shown in Figure 2. The footprint was then reduced by bringing the blocks closer (Antenna III) and finally merging them into a single cross-shaped dielectric

volume. The final geometry is obtained by optimizing the overlap between arms and the bent microstrip feeds to place the operating band around 28 GHz while maintaining low inter-port coupling (Figure 2).

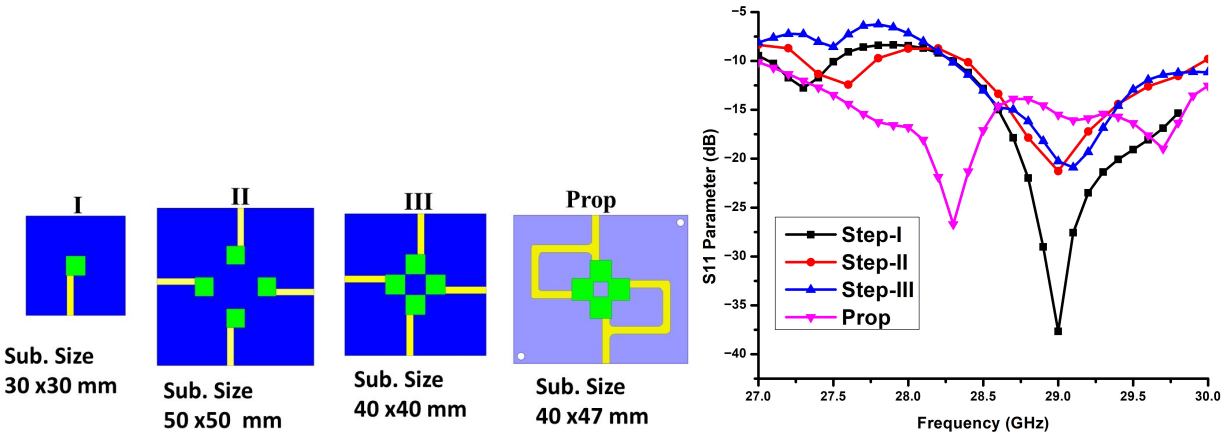

Figure 2. Design steps (**left**) and corresponding S parameters (**right**).

In the HFSS simulations, a bonding layer was incorporated between the dielectric resonator and the substrate to reflect practical fabrication conditions. A 5 µm-thick adhesive layer with relative permittivity $\varepsilon_r = 2.55$ was modeled, closely matching the substrate permittivity ($\varepsilon_r = 2.94$). A parametric sensitivity study was further performed with respect to the key geometrical parameters of the resonator (arm length, arm width, and height). The results confirm that minor dimensional variations preserve both the impedance and axial ratio bandwidths, indicating that the design is not overly sensitive to small fabrication tolerances.

2.3. Mode Analysis of the Dielectric Resonator

The operating mode is examined using eigenmode simulations of the parent RDRA and the final cross-shaped resonator. Figure 3 shows normalized Mag-E on the YZ and XZ planes of the standalone RDRA at $\omega t = 0°, 90°, 180°$, and 270° consistent with a quasi-TE^{z}_{311} mode predicted by the initial Marcatili-based sizing.

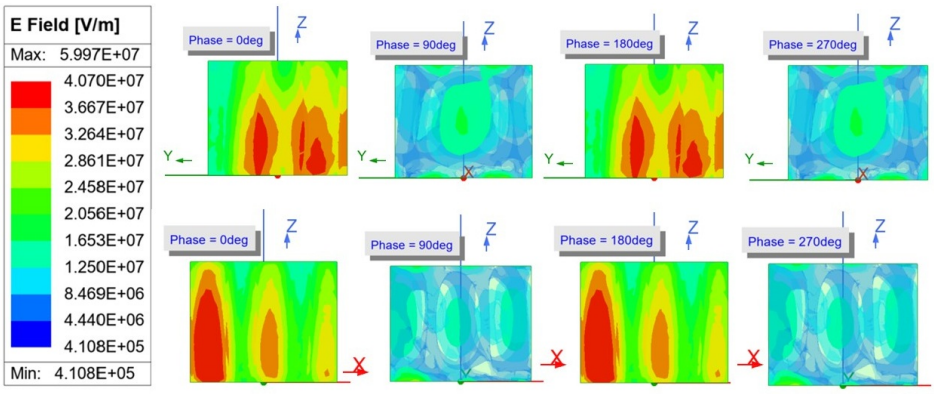

Figure 3. Eigenmode Mag-E of the parent RDRA at $\omega t = 0°, 90°, 180°, 270°$ on the YZ (**top**) and XZ (**bottom**) planes, showing a quasi-TE^{z}_{311}-type field distribution.

When four such RDRAs are merged into the cross-shaped resonator, the shared dielectric volume introduces coupling and perturbs the canonical field symmetry. As shown in Figure 4, the principal lobe signature is retained, but the field becomes distorted across the arms. The resonance is therefore described as a perturbed/hybrid TE-like mode derived from the quasi-TE_{311} family.

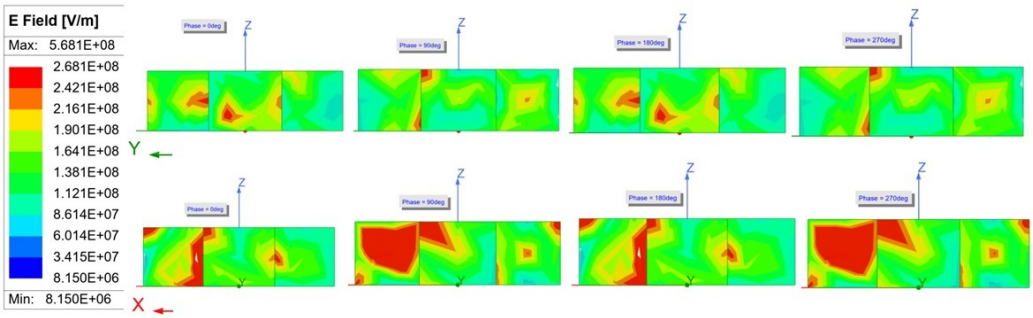

Figure 4. Eigenmode Mag-E of the cross-shaped dielectric resonator at $\omega t = 0°, 90°, 180°, 270°$ on the YZ (**top**) and XZ (**bottom**) planes, indicating a perturbed/hybrid TE-like mode derived from the quasi-TE_{311} family.

2.4. Working Principle and CP Generation

The circular polarization mechanism is illustrated in Figure 5. At 28.2 GHz, the instantaneous electric field vectors inside the resonator rotate with time at $\omega t = 0°, 90°, 180°$, and 270°, confirming that two orthogonal field components with comparable magnitude and near-quadrature phase are supported by the cross-shaped DRA. By mirroring the feed layout (Figure 6), the rotation sense reverses, providing LHCP or RHCP from the same resonator.

To further validate the circular polarization mechanism, the magnitude ratio and phase difference between the two orthogonal field components were extracted at 28.2 GHz. The magnitude ratio remains close to unity, and the phase difference approaches 90°, confirming the balanced excitation of near-degenerate orthogonal modes.

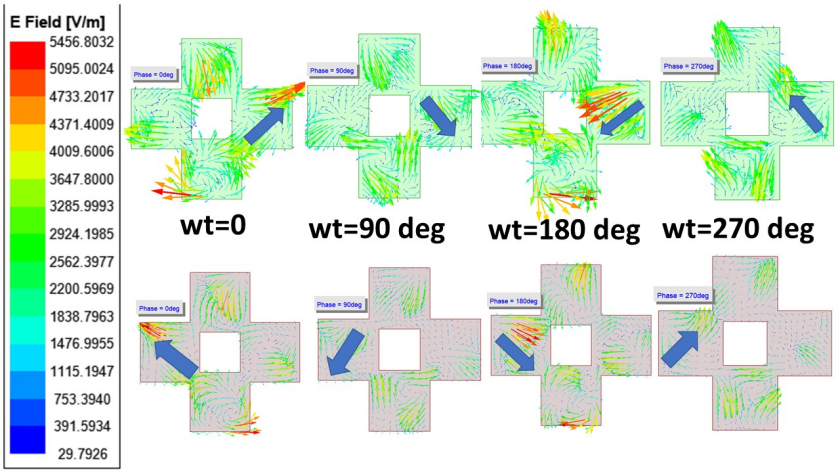

Figure 5. Simulated field snapshots at different time phases (at $\omega t = 0°, 90°, 180°, 270°$) showing LHCP (**top row**) and RHCP (**bottom row**) for the two feed configurations of Figure 6 at 28.2 GHz.

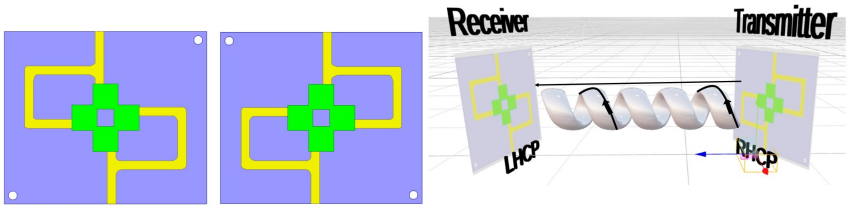

Figure 6. Two anti-symmetric feed layouts used to realize LHCP (**left**) and RHCP (**right**) with the same cross-shaped DRA.

3. Results and Discussion

3.1. Prototype and Measurement Setup

A prototype of the proposed dual-port DRA was fabricated and measured to validate the simulation results. Photographs of the realized structure are shown in Figure 7. The cross-shaped Eccostock Hik block was machined to the specified dimensions and bonded on top of the RT/Duroid 6002 substrate using a thin low-permittivity adhesive. The microstrip feed network and ground plane were realized using standard PCB etching, and 2.92 mm end-launch connectors were mounted at both ports.

Far-field measurements were carried out in a standard anechoic chamber, as illustrated in Figure 8. A standard linearly polarized waveguide horn antenna was used as the reference antenna and placed at a distance of 2.5 m from the antenna under test (AUT). During the measurement of one port, the other port was terminated with a 50 Ω matched load. A Keysight N5227A vector network analyzer was employed for both S-parameter and radiation pattern measurements.

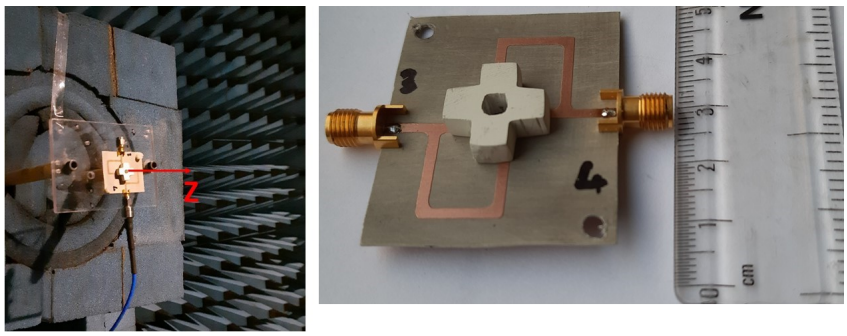

Figure 7. Fabricated prototype under test in anechoic chamber (**left**) and close-up view of the DRA with ruler (**right**).

Because the AUT is circularly polarized and the reference horn is linearly polarized, the orthogonal field components E_θ and E_ϕ were extracted by rotating the horn polarization. For each azimuth cut, $\phi = 0°$ and $\phi = 90°$, the AUT was kept fixed while the horn was sequentially aligned for horizontal and vertical polarizations, and the co-polarized responses were recorded over θ. The RHCP and LHCP components were then reconstructed from the complex combinations $(E_\theta \pm jE_\phi)$, and the axial ratio (AR) was obtained from their magnitude ratio. All post-processing was performed in MATLAB 2025.

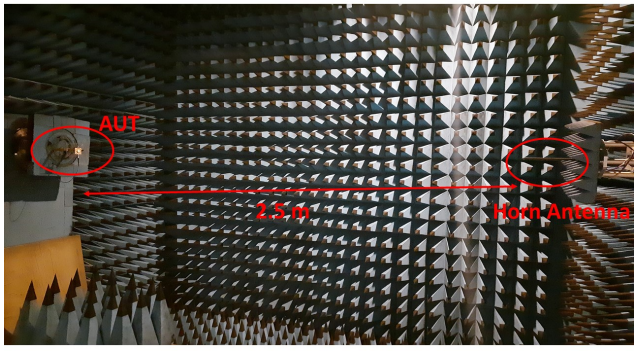

Figure 8. Measurement setup in the anechoic chamber. The AUT and the reference horn are separated by 2.5 m.

3.2. Impedance Bandwidth and Isolation

Figure 9 compares the simulated and measured S-parameters of the proposed antenna. As observed from the design evolution study in Figure 2, the simulated reflection coefficient

S_{11} exhibits a broad impedance bandwidth extending approximately from 27 to 30 GHz, satisfying the $|S_{11}| < -10$ dB criterion. This wide response confirms that the proposed resonator structure inherently supports broadband operation around the mmWave region. Since the present work specifically targets the FCC-allocated 28 GHz band (27.5–28.35 GHz), detailed measurements and discussion are focused on this frequency range. Accordingly, Figure 9 presents the simulated and measured S-parameters over the 27–29 GHz span, highlighting the antenna performance within and around the intended operating band. The measured S_{11} closely follows the simulated response, with a small frequency shift attributed to fabrication tolerances in the dielectric resonator dimensions and the adhesive bonding layer. A minimum measured reflection coefficient of approximately −42 dB is observed near 27.95 GHz. Due to the geometric and feeding symmetry of the antenna, the response at Port 2 is identical to that at Port 1; therefore, S_{22} is not plotted separately for clarity. The measured transmission coefficient S_{12} (and S_{21}) remains below −15 dB across 27–29 GHz, with a minimum near −40 dB close to the resonance. The achieved isolation level (>15 dB across the band) results primarily from orthogonal modal field distributions within the single dielectric volume and the comparatively weak induced currents on the orthogonal feed (see Figure 10) rather than external decoupling structures. While higher isolation can be obtained using EBG or parasitic elements, the present work prioritizes compactness and mechanical simplicity, offering isolation adequate for many mmWave MIMO front-end use cases while retaining a minimal complexity. Overall, both the simulation and measurement confirm an impedance bandwidth (IBW) fully covering the targeted 28 GHz band.

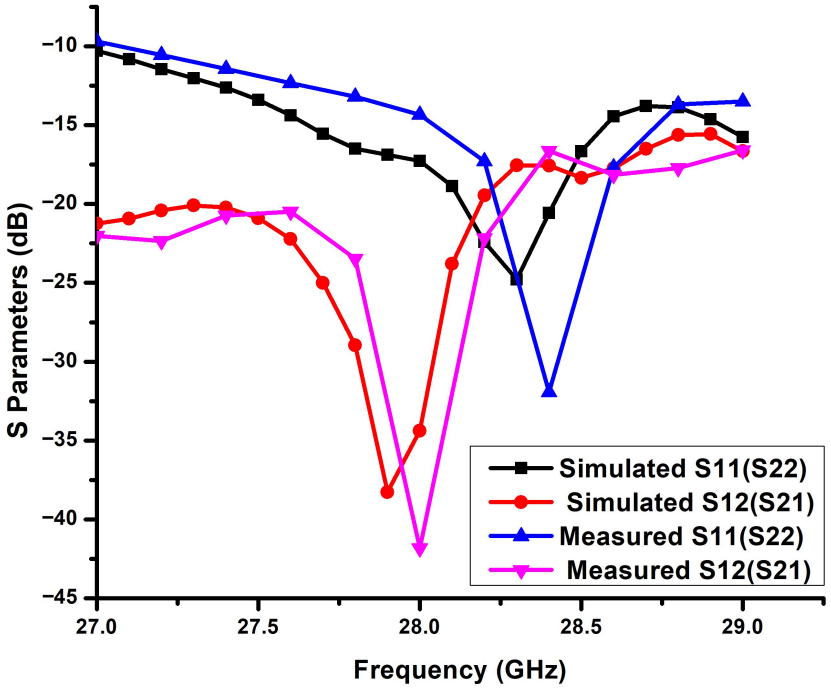

Figure 9. Simulated and measured S_{11} and S_{12} of the proposed dual-port DRA.

3.3. Axial Ratio, Gain, and Radiation Patterns

The simulated and measured 3 dB axial ratio responses are plotted in Figure 11. The simulated AR is below 3 dB from 27.5 to 28.75 GHz, with a minimum under 1 dB at approximately 28.2 GHz. The measured ARBW is slightly narrower, extending from 27.8 to 28.5 GHz (2.4%), and the minimum AR is about 1.2–1.5 dB. The small degradation and frequency shift arise due to manual placement tolerances of the DRA on board and measurement uncertainties.

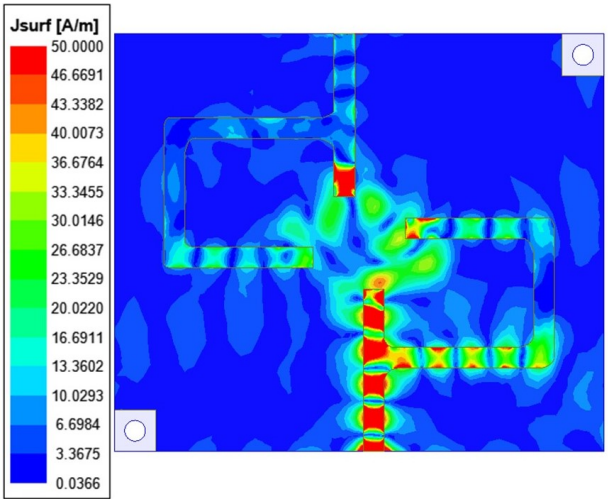

Figure 10. Simulated surface current distribution when one port is excited at 28.2 GHz.

3.4. Axial Ratio, Gain, and Radiation Patterns

The simulated and measured 3 dB axial ratio responses are plotted in Figure 11. The simulated AR is below 3 dB from 27.5 to 28.75 GHz, with a minimum under 1 dB at approximately 28.2 GHz. The measured ARBW is slightly narrower, extending from 27.8 to 28.5 GHz (2.4%), and the minimum AR is about 1.2–1.5 dB. The small degradation and frequency shift arise due to manual placement tolerances of the DRA on board and measurement uncertainties.

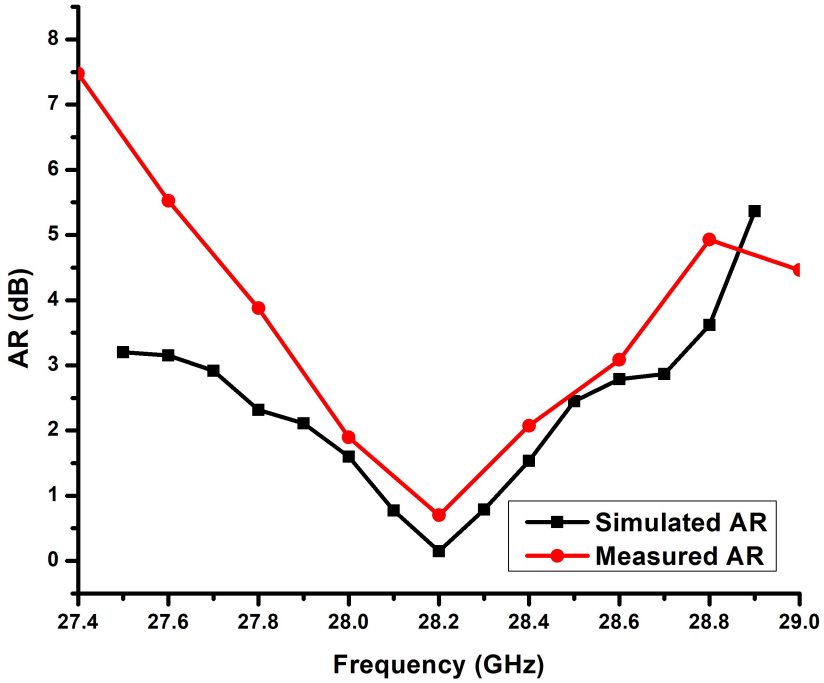

Figure 11. Simulated and measured axial ratio versus frequency.

The simulated radiation efficiency and gain within the AR window are depicted in Figure 12. The measured gain varies between about 5.5 dBi and 7 dBi whereas the maximum simulated gain was observed to be 7.56 dBi at 27.6 GHz. The simulated radiation efficiency remains high, around 93–94%, confirming that conductor and dielectric losses are well controlled despite the compact footprint and mmWave operation.

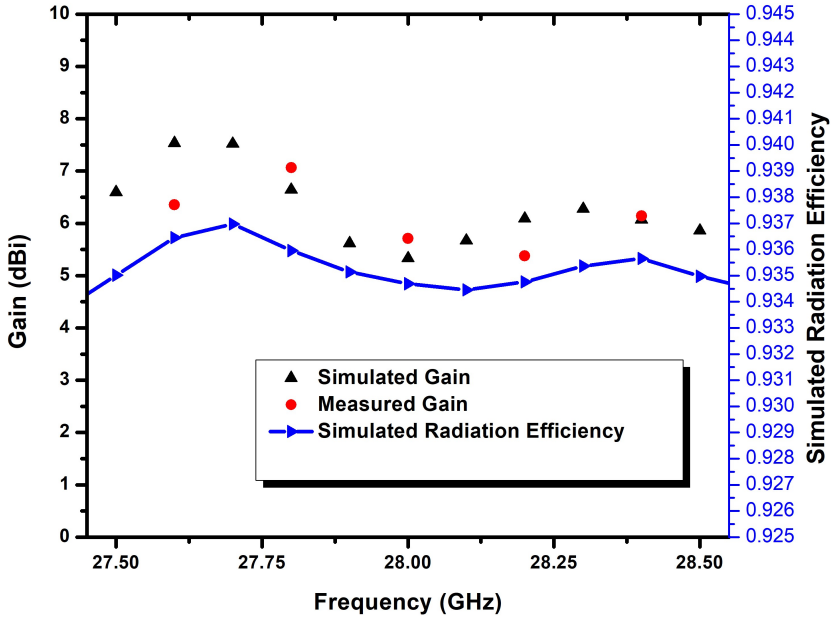

Figure 12. Simulated broadside gain and radiation efficiency of the proposed antenna.

Figure 13 shows the simulated and measured RHCP and LHCP radiation patterns at 28.2 GHz for $\phi = 0°$ and $\phi = 90°$. In both principal cuts, the RHCP component dominates around the broadside by more than 15 dB, confirming the correct sense of circular polarization. The measured main beams agree well with the simulations; slight asymmetries and elevated sidelobes, especially for a large negative θ, are attributed to the finite ground plane, coaxial connectors, and support fixtures. The cross-polarization level in the main beam region remains below -15 dB.

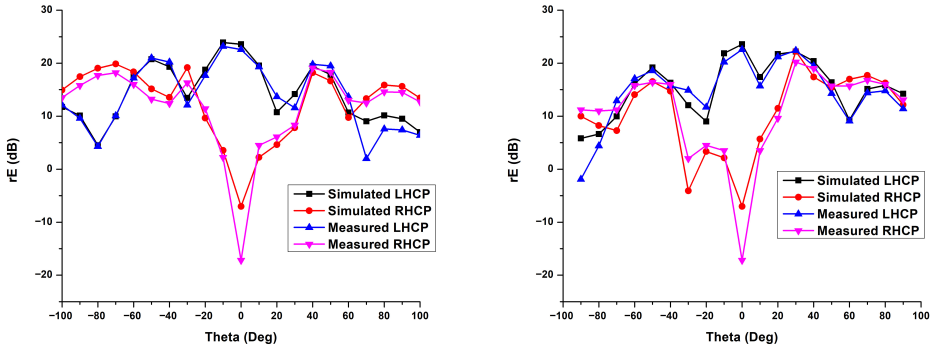

Figure 13. Simulated and measured radiation patterns of the proposed DRA at 28.2 GHz: $\phi = 0°$ plane (**left**) and $\phi = 90°$ plane (**right**).

3.5. MIMO Performance: ECC, Diversity Gain, and TARC

The envelope correlation coefficient (ECC) quantifies the statistical independence between radiation patterns associated with different antenna ports and is a key indicator of diversity performance in MIMO systems. The ECC can be evaluated either from S-parameters or directly from the far-field radiation patterns. For electrically small and directional antennas, particularly at mmWave frequencies, the radiation pattern-based formulation is generally more reliable, as it does not depend on accurate radiation efficiency estimation [11,12].

Accordingly, the ECC (ρ_{12}) is evaluated here using the far-field approach [13,14]:

$$\rho_{12} = \frac{\left| \iint_{4\pi} \left[\mathrm{XPR}\, E_{\theta 1} E_{\theta 2}^{*} P_{\theta} + E_{\phi 1} E_{\phi 2}^{*} P_{\phi} \right] d\Omega \right|^{2}}{\delta_1\, \delta_2}, \tag{1}$$

where

$$\delta_i = \iint_{4\pi} \left| \mathrm{XPR}\, E_{\theta i} E_{\theta i}^{*} P_{\theta} + E_{\phi i} E_{\phi i}^{*} P_{\phi} \right| d\Omega, \quad i = 1, 2. \tag{2}$$

Here $E_{\theta i}$ and $E_{\phi i}$ denote the elevation and azimuth components of the radiated electric field when port i is excited and the other port is terminated with 50 Ω; $(\cdot)^{*}$ represents the complex conjugate; $\mathrm{XPR} = P_V / P_H$ is the cross-polarization discrimination factor; and P_{θ} and P_{ϕ} are the angular power densities of the incoming waves.

For a rich isotropic scattering environment, it is customary to assume $P_{\theta} = P_{\phi} = 1/(4\pi)$ and $P_V = P_H$ [13,14]. Under these assumptions, the ECC is computed from the measured radiation patterns. As shown in Figure 14, the measured ρ_{12} remains below 0.3 across the 28 GHz band, reaching a minimum value of 0.05 near 28.2 GHz. The corresponding simulated ECC obtained from HFSS using the S-parameter formulation remains below 0.006 over the same band, confirming a very low correlation between the two ports.

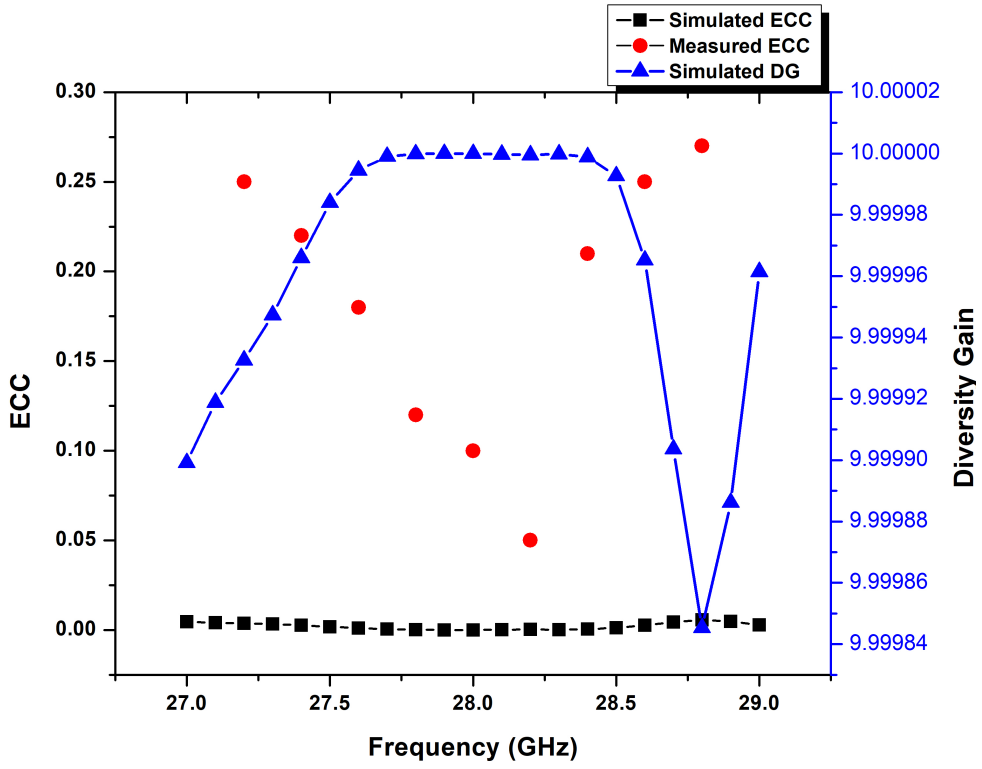

Figure 14. Simulated and measured envelope correlation coefficient and simulated diversity gain.

The diversity gain (DG), which reflects the effective improvement in link reliability due to diversity, is calculated as:

$$DG \approx 10\sqrt{1 - \rho_{12}^{2}}. \tag{3}$$

The resulting DG approaches 10 dB across the operating band, as also shown in Figure 14, indicating the excellent diversity performance of the proposed MIMO antenna.

Another important MIMO figure of merit is the total active reflection coefficient (TARC), which quantifies the amount of power reflected back to the ports when they are excited simultaneously with equal amplitudes and a phase difference θ [11]:

$$\mathrm{TARC} = \sqrt{\frac{\left(S_{11} + S_{12}e^{j\theta}\right)^2 + \left(S_{21} + S_{22}e^{j\theta}\right)^2}{2}}. \quad (4)$$

Figure 15 shows the simulated TARC as a function of frequency for several phase offsets θ. For all examined phase values, the TARC remains well below −20 dB across the 27–29 GHz band and exhibits deep minima close to resonance. These low values indicate that the majority of the input power is effectively radiated when both ports are active, confirming the suitability of the proposed antenna for MIMO operation.

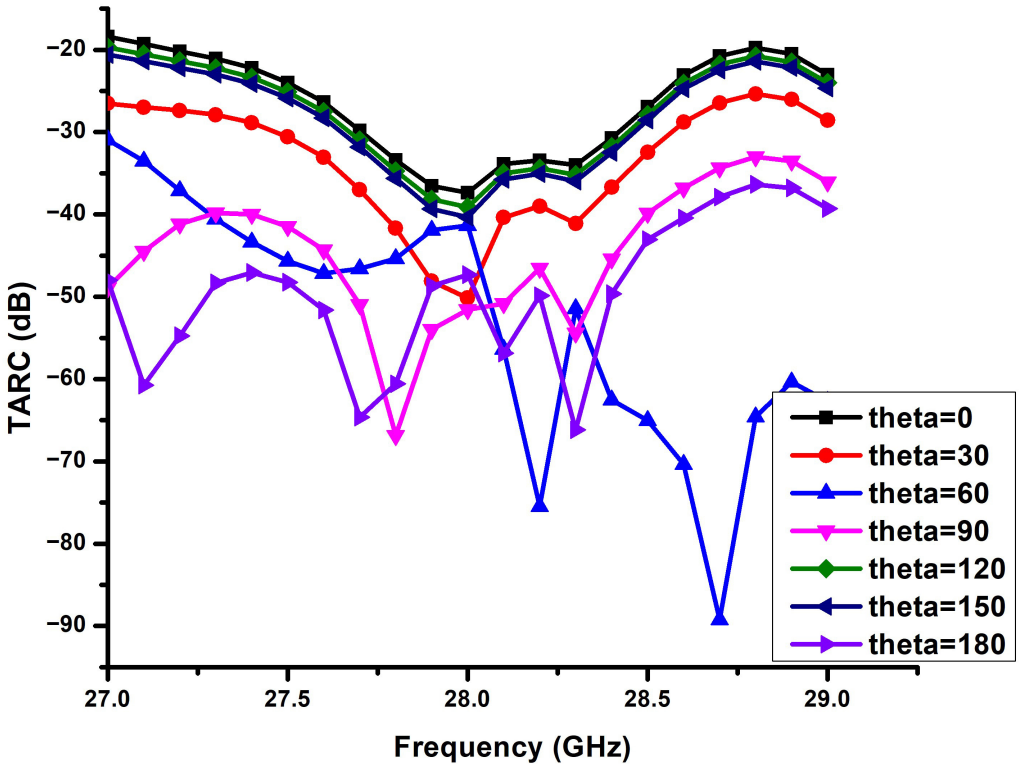

Figure 15. Simulated TARC versus frequency for different excitation phase differences θ.

3.6. Reconfigurable Polarization Using Anti-Symmetric Feeds

An additional feature of the proposed configuration is its ability to generate either LHCP or RHCP by simply mirroring the microstrip feed arrangement. Figure 6 shows two layouts with anti-symmetric feed lines. In one case, the structure radiates LHCP in the broadside direction, whereas in the mirrored configuration the same cross-shaped DRA radiates RHCP with almost identical gain and pattern characteristics. This property is illustrated in Figure 5, which presents the simulated instantaneous electric field distributions at different time phases for both configurations. The rotation of the field vectors clearly reverses when the feed symmetry is flipped. The field plots also reveal that the CP purity is slightly higher in one half of the cross-shaped resonator than in the other. The asymmetry is primarily associated with localized feed-induced perturbation and is most noticeable away from the principal radiation direction. In the main beam region, where practical mmWave terminal links operate, the circular polarization remains stable and well defined. To quantitatively validate the CP mechanism, the orthogonal modal balance was evaluated on the broadside by extracting the magnitude ratio $|E_\theta|/|E_\phi|$ and

the phase difference $\angle E_\theta - \angle E_\phi$ across the operating band. As illustrated in Figure 16, the magnitude ratio remains close to unity while the phase difference approaches $\pm 90°$ within the CP bandwidth, confirming near-degenerate orthogonal hybrid-mode excitation and stable circular polarization generation. Nonetheless, the CP quality remains within acceptable limits for practical 5G/6G MIMO terminals. Overall, the experimental results confirm that the proposed dual-port cross-shaped DRA achieves wide overlapping IBW and ARBW, a high radiation efficiency, a low port correlation, and favorable TARC behavior in a compact form factor, making it a strong candidate for polarization-diverse mmWave MIMO applications.

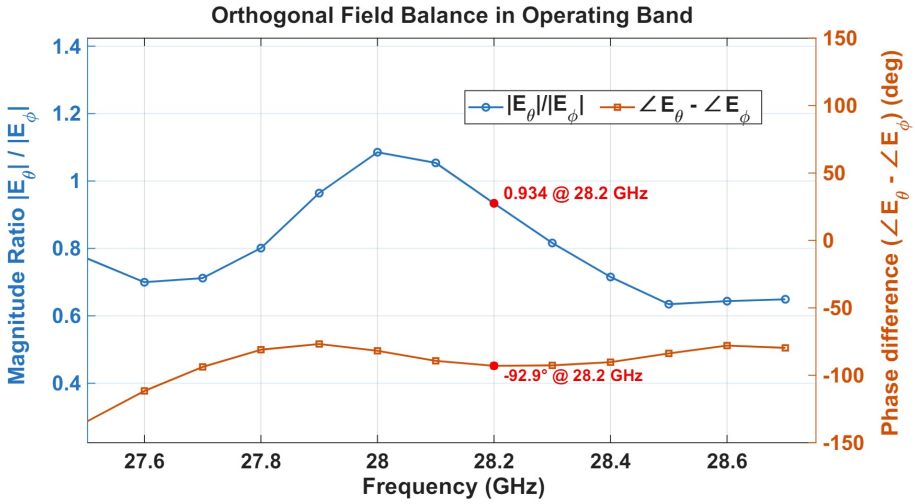

Figure 16. Simulated orthogonal-mode magnitude ratio ($|E_\theta|/|E_\phi|$) and phase difference($\angle E_\theta - \angle E_\phi$) versus frequency.

3.7. Comparison with Other CP MIMO DRAs

A wide range of circularly polarized MIMO DRA configurations has been explored in recent years, covering different operating bands and structural approaches. Most existing CP MIMO DRAs, however, are designed for sub-6 GHz operation and typically rely on more than one dielectric resonator or the inclusion of auxiliary structures to control mutual coupling and polarization purity. Representative examples include ring-shaped DRAs [7], hybrid multi-mode and dual-element DRA configurations [6,16], as well as designs incorporating electromagnetic bandgap layers, parasitic strips, or absorber-based isolation techniques [8–10]. While effective, these approaches increase structural complexity and footprint, which becomes increasingly restrictive when scaled to millimeter-wave frequencies. As per the authors' knowledge, only a limited number of DRA-based MIMO antennas have been reported at higher frequencies. Among the available designs, one operates directly in the 28 GHz band [17]; however, it is linearly polarized and therefore does not address circularly polarized MIMO operation. Other CP MIMO DRAs employing dual dielectric resonators and printed isolation elements have been demonstrated at lower microwave frequencies [18], but their overall dimensions and reliance on multiple resonant blocks make them unsuitable for 28 GHz applications. Similarly, dual-element CP MIMO DRAs reported in the literature [6,19] exhibit good performances in their respective bands, yet few are directly applicable to compact 28 GHz applications due to scaling limitations. The comparison shown in Table 1 clearly illustrate these trends. With the exception of the proposed antenna, all CP MIMO DRAs listed employ two or more resonators and/or additional isolation techniques such as defected ground structures (DGSs) [7,19], metameterial absorber layers [10], metallic strips [8,18], electromagnetic bandgap (EBG) surfaces [20], or parasitic elements [21].

Moreover, most operate well below 6 GHz. At mmWave frequencies, the only listed design near the 28 GHz band is linearly polarized [17]. In contrast, the proposed antenna achieves dual circular polarization within the 28 GHz band using a single cross-shaped dielectric resonator, without relying on external decoupling structures or additional resonators. This configuration maintains a compact footprint, provides port isolation better than 15 dB, and exhibits a high radiation efficiency (approximately 94%). The measured axial ratio bandwidth fully overlaps the 28 GHz allocation band, and the envelope correlation coefficient remains low across the operating band. Based on the available literature, the proposed design demonstrates that dual-port circular polarization at 28 GHz can be realized using a single resonant dielectric element, offering a compact and structurally simplified solution for 5G/6G applications.

Table 1. Comparison of recent circularly polarized MIMO DRAs.

Ref	IBW (GHz)	ARBW (GHz)	Gain (dBi)	Isolation (dB)	Rad Eff. (%)	No. of Elements	Feed	Isolation Technique
[6]	5.71–8.20	7.72–8.04	3.8	15	80	2	Conformal microstrip	Zero-spacing dual DRs
[7]	2.3–2.9, 3.4–4.0	3.45–3.80	3.0, 4.0	20	90	2	Modified plus-slot	DGS
[8]	2.70–3.20	2.7–3.10	4.3	38	–	2	Slot-fed	Z-strip + metallic vias
[9]	3.22–3.72	3.34–3.54	4.2	>15	–	4	Slot + loop	Polarization diversity
[10]	5.00–5.80	5.27–5.50	5.1	28	90	4	Unbalanced slot	Metamaterial absorber
[16]	3.15–3.90	3.26–3.45	7.3	20	90	2	Dual conformal probes	Ground slots
[17]	27.19–28.48	–	–	24	–	2	Slot-fed	Top metal strip
[18]	2.36–2.59	2.39–2.51	5.6	22	–	2	Cross-slot	Lateral metal strips
[19]	3.10–3.75, 5.30–5.60	3.42–3.60, 5.45–5.55	6.8, 4.6	16	–	2	Arc microstrip + probes	DGS
[20]	3.15–3.93	3.30–3.80	4.83	26	–	2	Cross-ring slot	EBG surface
[21]	3.50–4.95	3.58–4.40	6.2	26	–	2	E conformal strip	Parasitic patch + diagonal placement of DRs
This Work	27–29	27.5–28.75	7.56	>15	94	1	Orthogonal microstrip	Cross-shaped DR

4. Conclusions

A compact dual-port circularly polarized MIMO DRA suitable for 28 GHz band applications has been presented. The cross-shaped DRA, realized from a single ceramic block on an RT/Duroid 6002 substrate, is excited by orthogonal microstrip lines. The antenna exhibits IBW and ARBW which fully covers the Federal Communications Commission (FCC)-allocated 28 GHz band. Port isolation exceeds 15 dB, ECC is below 0.3 in the band of interest, and TARC remains well below -20 dB for all excitation phases. The design is mechanically robust thanks to the screw holes and planar feed implementation. By realizing dual-port circular polarization using a single resonator without additional decoupling or perturbation structures, the proposed design offers a compact, mechanically robust,

and integration-friendly solution for mmWave MIMO applications in 5G and 6G wireless terminals. The compact single-resonator configuration makes the antenna suitable for integration in polarization-diverse 2 × 2 phased-array modules, compact mmWave access points, and small-cell units where space and structural simplicity are critical.

Author Contributions: Conceptualization, S.S.S. and L.M.; methodology, S.S.S.; software, S.S.S.; validation, S.S.S. and L.M.; formal analysis, S.S.S.; investigation, S.S.S.; resources, S.S.S.; data curation, S.S.S.; writing—original draft preparation, S.S.S.; writing—review and editing, S.S.S. and L.M.; visualization, S.S.S.; supervision, L.M.; project administration, S.S.S.; funding acquisition, S.S.S. and L.M. All authors have read and agreed to the published version of the manuscript.

Funding: This study was supported by the European Union–NextGenerationEU, under the Italian National Recovery and Resilience Plan (NRRP), Mission 4 Component 2 Investment 1.2, funding scheme "Young Researchers" (D.D. 201 del 3.7.2024) CUP E13C24002390006.

Data Availability Statement: All relevant data are included in this article.

Conflicts of Interest: The authors declare no conflicts of interest.

References

1. Federal Communications Commission. 28 GHz Band: Auction 101 Factsheet. 2018. Available online: https://www.fcc.gov/auction/101 (accessed on 14 November 2025).
2. Luk, K.M.; Leung, K.W. *Dielectric Resonator Antennas*; Research Studies Press: Hertfordshire, UK, 2003.
3. Petosa, A. *Dielectric Resonator Antenna Handbook*; Artech House: Norwood, MA, USA, 2007.
4. Mongia, R.K.; Bhartia, P. Dielectric resonator antennas—A review and general design relations for resonant frequency and bandwidth. *Int. J. RF Microw. Comput.-Aided Eng.* **1994**, *4*, 230–247. [CrossRef]
5. Mongia, R.K.; Ittipiboon, A. Theoretical and experimental investigations on rectangular dielectric resonator antennas. *IEEE Trans. Antennas Propag.* **1997**, *45*, 1348–1356. [CrossRef]
6. Varshney, G.; Singh, R.; Pandey, V.S.; Yaduvanshi, R.S. Circularly polarized two-port MIMO dielectric resonator antenna. *Prog. Electromagn. Res. M* **2020**, *91*, 19–28. [CrossRef]
7. Bharti, G.; Kumar, D.; Gautam, A.K.; Sharma, A. Two-port ring-shaped dielectric resonator-based diversity radiator with dual-band and dual-polarized features. *Microw. Opt. Technol. Lett.* **2020**, *62*, 581–588. [CrossRef]
8. Elahi, M.; Joung, J.; Lim, S. Isolation and bandwidth enhancement in compact CP MIMO DRA in H-plane using Z-shaped strip. *IEEE Antennas Wirel. Propag. Lett.* **2023**, *22*, 2700–2704. [CrossRef]
9. Sahu, N.K.; Das, G.; Gangwar, R.K.; Rambabu, K. An arrangement for four-element MIMO DRA with complementary CP diversity. *IEEE Antennas Wirel. Propag. Lett.* **2021**, *20*, 1616–1620. [CrossRef]
10. Kumari, T.; Suman, K.K.; Gangwar, R.K.; Chaudhary, R.K. Metamaterial absorber-integrated CP MIMO DRA for EMI reduction and high isolation. *IEEE Lett. Electromagn. Compat. Pract. Appl.* **2025**, *7*, 73–78. [CrossRef]
11. Sharawi, M.S. Current misuses and future prospects for printed multiple-input, multiple-output antenna systems. *IEEE Antennas Propag. Mag.* **2017**, *59*, 162–170. [CrossRef]
12. Sharawi, M.S.; Hassan, A.T.; Khan, M.U. Correlation coefficient calculations for MIMO antenna systems: A comparative study. *Int. J. Microw. Wirel. Technol.* **2017**, *9*, 1991–2004. [CrossRef]
13. Elshirkasi, A.M.; Al-Hadi, A.A.; Mansor, M.F.; Khan, R.; Soh, P.J. Envelope correlation coefficient of a two-port MIMO terminal antenna under uniform and Gaussian angular power spectrum with user's hand effect. *Prog. Electromagn. Res. C* **2019**, *92*, 123–136. [CrossRef]
14. Singhwal, S.S.; Kanaujia, B.K.; Singh, A.; Kishor, J. Dual-port MIMO dielectric resonator antenna for WLAN applications. *Int. J. RF Microw. Comput.-Aided Eng.* **2020**, *30*, e22108. [CrossRef]
15. Marcatili, E.A.J. Dielectric rectangular waveguide and directional coupler for integrated optics. *Bell Syst. Tech. J.* **1969**, *48*, 2071–2102. [CrossRef]
16. Singhwal, S.S.; Kanaujia, B.K.; Singh, A.; Kishor, J.; Matekovits, L. Multiple-input multiple-output dielectric resonator antenna with circular polarized adaptability for 5G applications. *J. Electromagn. Waves Appl.* **2020**, *34*, 1180–1194. [CrossRef]
17. Zhang, Y.; Deng, J.-Y.; Li, M.-J.; Sun, D.; Guo, L.-X. A MIMO dielectric resonator antenna with improved isolation for 5G mm-wave applications. *IEEE Antennas Wirel. Propag. Lett.* **2019**, *18*, 747–751. [CrossRef]
18. Hu, Y.; Pan, Y.M.; Yang, M.D. Circularly polarized MIMO dielectric resonator antenna with reduced mutual coupling. *IEEE Trans. Antennas Propag.* **2021**, *69*, 3811–3820. [CrossRef]

19. Singhwal, S.S.; Kanaujia, B.K.; Singh, A.; Kishor, J.; Matekovits, L. Dual-band circularly polarized MIMO DRA for sub-6 GHz applications. *Int. J. RF Microw. Comput.-Aided Eng.* **2020**, *30*, e22350. [CrossRef]
20. Chen, H.N.; Song, J.-M.; Park, J.-D. A compact circularly polarized MIMO dielectric resonator antenna over electromagnetic band-gap surface for 5G applications. *IEEE Access* **2019**, *7*, 140889–140898. [CrossRef]
21. Iqbal, J.; Illahi, U.; Sulaiman, M.I.; Alam, M.M.; Su'ud, M.M.; Yasin, M.N.M. Mutual coupling reduction using hybrid technique in wideband circularly polarized MIMO antenna for WiMAX applications. *IEEE Access* **2019**, *7*, 40951–40958. [CrossRef]